Velocity map imaging study of the photodissociation dynamics of the allyl radical†

Marta G. González,^{a} Sonia Marggi Poullain,^{a,b} Luis Rubio-Lago,^{a} and Luis Bañares^{*a,c}

The photodissociation of the allyl radical (CH$_2$=CH–CH$_2^\bullet$) following excitation between 216 and 243 nm has been investigated employing velocity map imaging in conjunction with resonance enhanced multiphoton ionization to detect the hydrogen atom and CH$_3$(v=0) produced. The translational energy distributions for the two fragments are reported and analyzed along with the corresponding fragment ion angular distributions. The results are discussed in terms of the different reactions pathways characterizing the hydrogen atom elimination and the minor methyl formation. On one hand, the angular analysis provides evidence of an additional mechanism, not reported before, leading to prompt dissociation and fast hydrogen atoms. On the other hand, the methyl elimination channel has been characterized as a function of the excitation energy and the contribution of three reaction pathways: single 1,3-hydrogen shift, double 1,2-hydrogen shift and formation of vinylidene have been discussed. Contrary to previous predictions, the vinylidene channel, which plays a significant role at lower energies, seems to vanish following excitation on the $\widetilde{E}\,^2B_1(3p_x)$ excited state at $\lambda \leq 230$ nm.
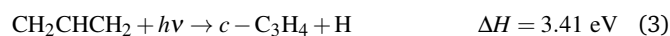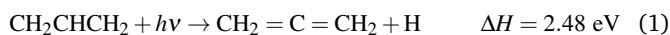
1 Introduction

The allyl radical (CH$_2$=CH–CH$_2^\bullet$) constitutes the simplest hydrocarbon radical characterized by a conjugated π bond system. Besides the fundamental interest, allyl radical photochemistry has attracted a lot of interest due to its presence in reactive environments such as interstellar space [1–3] and its role in combustion processes [4–7]. It is also an important precursor for the formation of cyclic molecules, such as benzene [8,9].

The absorption spectrum of the allyl radical is characterized by a first absorption band lying between 410 and 370 nm, corresponding to the transition from the $\widetilde{X}\,^2A_2$ ground state to the $\widetilde{A}\,^2B_1$ first excited state [10,11]. A second absorption band with a maximum around 222 nm is observed between 250 and 210 nm, where several excited states have been identified: the $\widetilde{B}\,^2A_1(3s)$, $\widetilde{C}\,^2B_2(3p_y)$ and $\widetilde{D}\,^2A_1(3p_z)$ located at 249.7 nm, 240.6 nm and 236.8 nm, respectively [12–15]. An additional diffuse band between 230.9 and 222 nm has been assigned to the $\widetilde{E}\,^2B_1(3p_x)$ excited state. The electronic states identified in the absorption spectra are summarized in Table 1. One-photon absorption into the $\widetilde{B}\,^2A_1$ and $\widetilde{D}\,^2A_1$ states is forbidden by symmetry although vibrational activity can allow the transitions. A large number of vibronic bands of the $\widetilde{B}\,^2A_1$ state have been reported in the measured (1+1) resonance enhanced multiphoton ionization (REMPI) spectra, while the $\widetilde{D}\,^2A_1$ state has been instead observed via two-photon absorption.

Different experimental investigations employing pump-probe schemes and time-of-flight spectrometry in conjunction with several theoretical studies including Rice-Ramsperger-Kassel-Marcus (RRKM) calculations and *ab initio* on-the-fly trajectories have been reported concerning the allyl dissociation dynamics leading to a major H-atom loss and to a minor methyl channel ($\sim$ 5%) [16–22].

In a recent publication by Zhang and co-workers [22], an overview of the literature on the allyl photochemistry and on the different reaction pathways is detailed in the introduction section. In brief, the H-atom loss channel has been attributed to a slow statistical dissociation following internal conversion from excited states to the ground state. Three main reaction pathways have been proposed:

$$\mathrm{CH_2CHCH_2} + h\nu \rightarrow \mathrm{CH_2}=\mathrm{C}=\mathrm{CH_2} + \mathrm{H} \qquad \Delta H = 2.48 \text{ eV} \quad (1)$$

$$\mathrm{CH_2CHCH_2} + h\nu \rightarrow \mathrm{CH}\equiv\mathrm{C}-\mathrm{CH_3} + \mathrm{H} \qquad \Delta H = 2.43 \text{ eV} \quad (2)$$

$$\mathrm{CH_2CHCH_2} + h\nu \rightarrow c-\mathrm{C_3H_4} + \mathrm{H} \qquad \Delta H = 3.41 \text{ eV} \quad (3)$$

^{a} *Departamento de Química Física, Facultad de Ciencias Químicas, Universidad Complutense de Madrid, 28040 Madrid, Spain. Tel: +34 913944228; E-mail: lbanares@ucm.es*

^{b} *Department of Chemistry, University of California at Berkeley, Berkeley, CA94720, USA*

^{c} *Instituto Madrileño de Estudios Avanzados en Nanociencia (IMDEA-Nanoscience), Cantoblanco, 28049 Madrid, Spain*
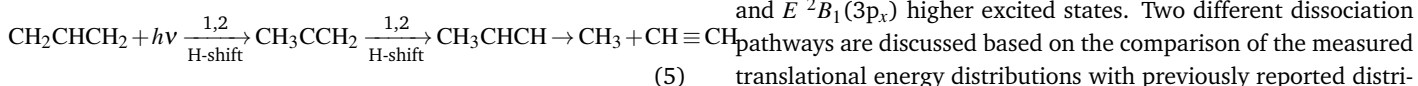
Table 1 Left columns: first electronic states of the allyl radical and wavelength λ location in the reported absorption spectra based on Ref.[15]. Middle and right columns: experimental excitation wavelengths (λ_{exp}) selected for the detection of H-atom and CH_3 fragments along with the corresponding electronic state initially excited according to the absorption spectrum[15]. The known vibronic transitions involving the C-C-C bending mode (v_7), the CH_2 out-of-plane bending mode (v_{11}) and the CH_2 twisting mode (v_{12}) for excitation at 238, 240 and 243 nm are also specified.

CH_2CHCH_2 Electronic States (ES)	λ / nm	λ_{exp} / nm (H-fragment)	Excited State	λ_{exp} / nm (CH_3-fragment)	Excited State
$\widetilde{X}\,^2A_2$	–	218	$\widetilde{E}\,^2B_1$	216	$\widetilde{E}\,^2B_1$
$\widetilde{A}\,^2B_1$	408.3	226	$\widetilde{E}\,^2B_1$	218	$\widetilde{E}\,^2B_1$
$\widetilde{B}\,^2A_1$	249.7	228	$\widetilde{E}\,^2B_1$	220	$\widetilde{E}\,^2B_1$
$\widetilde{C}\,^2B_2$	240.6	235	$\widetilde{D}\,^2A_1\,/\,\widetilde{C}\,^2B_2$	230	$\widetilde{E}\,^2B_1$
$\widetilde{D}\,^2A_1$	236.8	238	$\widetilde{C}\,^2B_2\ 7_0^1/12_0^2$	238	$\widetilde{C}\,^2B_2\ 7_0^1/12_0^2$
$\widetilde{E}\,^2B_1$	230.9-222	243	$\widetilde{B}\,^2A_1\ 11_0^1$	240	$\widetilde{C}\,^2B_2 \approx 0_0^0$

Besides the direct dissociation into allene (CH_2CCH_2) + H according to Eq. (1), which is the most favorable channel, it can also involve isomerization to 2-propenyl (CH_3CCH_2) followed by dissociation to allene. In addition, the formation of propyne (CH_3CCH) in Eq. (2) can occur through three different isomerization channels followed by dissociation to propyne: (*i*) from allyl to 2-propenyl, (*ii*) from allyl to 1-propenyl (CH_3CHCH) or (*iii*) from allyl to 2-propenyl and then to 1-propenyl. The allyl radical can also isomerize to the cyclopropyl radical which leads to the c-C_3H_4 + H products according to Eq. (3). A potential energy diagram showing the stationary points of these possible channels based on theoretical calculations is depicted in Figure 1 of Ref.[22].

Most experiments regarding the H-atom loss have been carried out following excitation on the first absorption band, between 351 and 420 nm, populating the $\widetilde{A}\,^2B_1$ excited state, and at 248 nm, just above the $\widetilde{B}\,^2A_1$. A recent investigation by Song *et al.*[22] has been reported on the UV photodissociation into H-atom loss following excitation between 249 and 219 nm to the $\widetilde{B}\,^2A_1(3s)$, $\widetilde{C}\,^2B_2(3p_y)$, $\widetilde{D}\,^2A_1(3p_z)$ and $\widetilde{E}\,^2B_1(3p_x)$ excited states. The photodynamics in these $\widetilde{B}\,^2A_1(3s)$, $\widetilde{C}\,^2B_2(3p_y)$ and $\widetilde{D}\,^2A_1(3p_z)$ higher excited states can be particularly interesting: a three-state same-symmetry conical intersection located above the $\widetilde{D}$ state was theoretically predicted by Yarkony and Matsika[23]. Two supplementary linked two-state conical intersections, one of which approaches the equilibrium geometry of the $\widetilde{B}$ state, were also reported. The results presented by Song *et al.*[22] were nevertheless similarly consistent with an internal conversion into the ground electronic state followed by slow unimolecular dissociation.

In contrast to the H-atom channel, the methyl-loss dissociation pathways have received much less attention. Stranges and co-workers[19–21] reported joint experimental and theoretical work on this channel at 248 nm, involving classical trajectories calculations on the ground state *ab initio* potential energy surface. Three mechanisms have been proposed:

$$CH_2CHCH_2 + h\nu \xrightarrow{\text{1,3 H-shift}} CH_3CHCH \rightarrow CH_3 + CH \equiv CH \quad (4)$$

$$CH_2CHCH_2 + h\nu \xrightarrow[\text{H-shift}]{1,2} CH_3CCH_2 \xrightarrow[\text{H-shift}]{1,2} CH_3CHCH \rightarrow CH_3 + CH \equiv CH \quad (5)$$

$$CH_2CHCH_2 + h\nu \xrightarrow{\text{1,2 H-shift}} CH_3CCH_2 \rightarrow CH_3 + CCH_2 \quad (6)$$

A scheme showing the local minima (LM) and transition states (TS) previously computed and relevant for the formation of CH_3 is depicted in Figure 1. The three possible dissociation channels[21] according to Eqs. (4)-(6) are indicated. As displayed by the blue line in Fig. 1, the first mechanism (Eq. (4)) involves a 1,3-hydrogen shift leading to the 1-propenyl intermediate, followed by a C-C cleavage to produce methyl and acetylene. In the second mechanism (Eq. (5) and green line in Fig. 1), two 1,2 hydrogen shifts are involved: from allyl to 2-propenyl and then to 1-propenyl, which similarly dissociates into methyl and acetylene. A third channel[20] (Eq. (6) and red line in Fig. 1) at higher energy produces methyl and vinylidene (C=CH_2) through the 2-propenyl isomer. This route, presenting similarities with the roaming mechanism, is characterized by a very *loose* transition state (TS5) which may favor it despite its high energy[20]. Vinylidene would then likely undergo further isomerization into acetylene.

In this work, we revisit the photodissociation of the allyl radical following excitation between 216 and 243 nm in a experimental pump-probe study employing resonance enhance multiphoton ionization (REMPI) and velocity map imaging of the H-atom and methyl fragments. The different selected excitation wavelengths employed while detecting each fragment are summarized in Table 1 along with the corresponding excited state populated according to the reported absorption spectrum. The populated vibronic bands are suggested according to Ref.[15]. The state populated following excitation at 235 nm is rather uncertain since, as mentioned above, the $\widetilde{D}$ state does not appear to be populated *via* a one-photon transition. The results presented in this work concerning the H-atom channel are carefully compared to those published by Song *et al.*[22] The angular analysis of the recorded H-atom images indicates a supplementary prompt dissociation channel, not reported before. In addition, this is, to the best of our knowledge, the first experimental study regarding the methyl channel at $\lambda < 248$ nm, *i.e.* exciting into $\widetilde{C}\,^2B_2(3p_y)$, $\widetilde{D}\,^2A_1(3p_z)$ and $\widetilde{E}\,^2B_1(3p_x)$ higher excited states. Two different dissociation pathways are discussed based on the comparison of the measured translational energy distributions with previously reported distri-
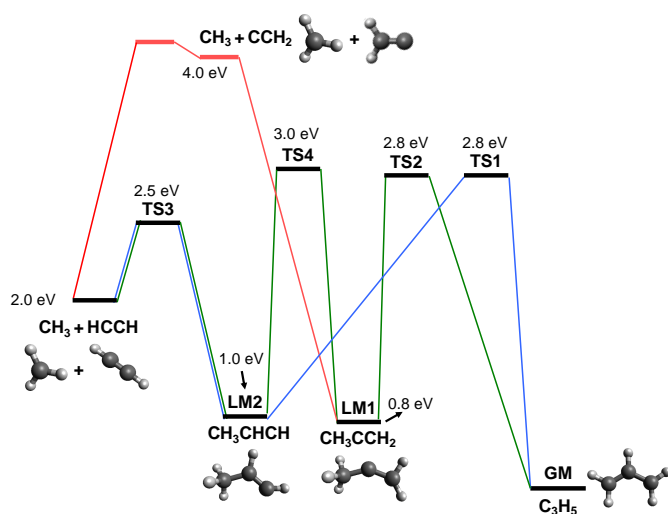
Fig. 1 Schematic representation of the reaction pathways in the dissociation of the allyl radical (CH_2CHCH_2) that correlate with the formation of CH_3 fragments. The relevant global minimum (GB), transition states (TS) and local minima (LM) are included and the corresponding energies from Ref. [19,20] are specified. Adapted from Ref. [21].

butions obtained from quasi-classical trajectories [20,21]. The article is organized as follows: in Section 2 the experimental method is briefly summarized while the results are presented and discussed in Section 3. The main conclusions of this work are given in Section 4.

2 Experimental method

The main characteristics of the experimental set-up have been described in detail before. [24,25] The whole experiment runs at a repetition rate of 10 Hz. The cold supersonic beam of allyl radicals is generated by flash pyrolysis of allyl iodide. The precursor was seeded in Helium (10%, 1 atm backing pressure) and expanded into vacuum using a pulsed nozzle (General Valve Series 9, 0.5 mm orifice) with a heated SiC tube mounted at the exit [17,26,27]. The gas pulse produced in the expansion goes through a skimmer (Beam Dynamics, Standard Model 2, 0.5 mm diameter orifice) and reaches the ionization chamber where the molecular beam is intersected in the middle of the electrical plates of a time-of-flight (TOF) mass spectrometer, by the photolysis and probe laser pulses, which are focused (f=25 cm) and counter propagated to each other.

In order to generate the photolysis laser radiation, a sum-frequency mixing nonlinear crystal is used to combine the fundamental wavelength, between 558 and 654 nm, of a dye laser (Sirah Cobra-Stretch) pumped by a Nd:YAG (Quanta Ray Pro 230) at 532 nm with the second harmonic of the same Nd:YAG laser at 355 nm. The excitation wavelengths were scanned between 216 and 243 nm and measured using a wavemeter (Wavemaster Coherent). The photoproducts are resonantly ionized 10-15 ns later via (2 + 1) REMPI schemes, using a focused probe pulse ($\approx$ 1.5 mJ per pulse) generated by a Nd:YAG (Quanta

Ray Pro 190) pumped frequency doubled dye laser (Sirah Cobra-Stretch). For $CH_3(v$=$0)$ detection, the probe laser wavelength was set at 333.45 nm, centered at the Q branch of the $3p_z$ $(^2A_2 \leftarrow ^2A_2)$ 0^0_0 transition for the two-photon process. For the detection of the hydrogen atoms, the probe laser wavelength was set at 243.1 nm which corresponds to the $2s(^2S_{1/2}) \leftarrow 1s(^2S_{1/2})$ two-photon transition. Due to the high velocity of the H-atom photofragments, the laser bandwidth used to excite the $2s \leftarrow 1s$ transition is narrower than the Doppler profile. In order to record all the velocities with similar probabilities, the probe laser was scanned over the Doppler profile of the transition during the experiments.

The H^+ and CH_3^+ images are recorded using a velocity map imaging (VMI) apparatus in the single-field configuration. [28] The generated H^+ and CH_3^+ ions are accelerated by an electric potential of 5 kV and 6.5 kV, respectively, applied to the repeller plate before passing through a field-free TOF region (45 cm) and hitting the impedance matched microchannel plates (MCPs) (Chevron configuration, 40 mm diameter). The gain of the MCPs can be gated with a high voltage pulse to allow only the ions of interest to be detected. An effective 10 ns detector gate of 500 V was applied on the front MCP to discriminate the other masses. The resulting electron avalanche strikes a phosphor screen (P47), thereby creating the ion image, which is recorded using a charged-coupled device (CCD) camera (SONY 1024 x 768 pixel), controlled using National Instruments (NI) LABVIEW 7.1 and IMAQ VISION software and analyzed with a commercial software (DAVIS). The final image is obtained as the sum of around 40 000 laser shots depending on the quality of the signal.

The images are quadrant symmetrized and Abel inverted using the Hankel transform prior to extracting the translational energy and angular distributions. Independent velocity-radius calibration of the apparatus is done by measuring resonantly ionized $CH_3(v$=$0)$ fragments produced after the photodissociation of CH_3I at 333.45 nm (one color pump-probe experiment) at different repeller potentials, taking advantage of the well known kinetic energy release of the $I(^2P_{3/2})$ yielding channel at this photolysis wavelength. [24]

3 Results and discussion

3.1 The H-atom elimination channels

Figure 2 presents a series of raw images recorded for H-atoms from the photodissociation of the allyl radical at different photolysis wavelengths ranging between 218 and 243 nm and detected via (2+1) REMPI at 243.1 nm. We note that the probe contribution and the background signal associated to the pyrolytic source have been carefully subtracted.The pump-probe signal represents around 3-4 times the probe and the background signals while the pump signal is negligible. The raw images prior subtraction at 228 nm are shown as an example in the ESI. All images reported here have been recorded employing a X(pump)X(probe) configuration where the polarization of both lasers is perpendicular to the laser propagation axis (parallel to the detector plane). Additional images employing a perpendicular configuration of both lasers (Z(pump)Z(probe)), where the polarization is parallel to

the molecular beam, *i.e.* perpendicular to the detector plane, have also been performed in order to detect possible inhomogeneities in the image. This is particularly relevant here in order to provide an accurate analysis of the angular distributions from the measured images.

The corresponding H-atom translational energy distributions (TED) obtained from Abel inversion and angular integration of the images are depicted in Figure 3. A quasi-isotropic blot in the images depicted in Figure 2 is observed at all wavelengths leading to a Boltzmann-type distribution in the corresponding TED. These results reflecting slow statistical dissociation pathways are pretty consistent with previous experimental TEDs reported by Song *et al.*[22] in the 216-249 nm range as well as with theoretical predictions published by Stranges and co-workers[21] following excitation at 248 nm.

Vertical bars in Fig. 3 represent the available energy E_{av} for the three opened dissociation channels c-C_3H_4 + H [Eq. (3)], CH_2CCH_2 + H [Eq. (1)]] and CH_3CCH + H [Eq. (2)] derived from $E_{av} = h\nu - D_0$, where $h\nu$ represents the excitation energy and D_0 is the corresponding dissociation energy, *i.e.* 3.41 eV, 2.48 eV and 2.43 eV, respectively. The abscissa axis in Fig.3 has been normalized to the available energy E_{av} characterizing the CH_3CCH + H dissociation channel in order to facilitate the comparison between different excitation wavelengths. The axis represents thus the fraction of the available energy channeled into translational energy, considering this CH_3CCH + H channel as reference, so that a $x=1$ value correlates to the E_{av} of this channel. As it can be observed, all three channels are energetically accessible and it is therefore not possible to determine the contribution of each channel from the present experiments. The distributions are characterized by an averaged translational energy $< E_T >$ around 0.55-0.60 eV, and a tail lasting up to $E_T \simeq 2$ eV, while in all cases they appear particularly shifted to the left, *i.e.* at lower translational energies, which reflects a high internal energy of the co-fragment. This behavior is indeed characteristic of a statistical dissociation.

Pixel-to-pixel radial integration of the Abel-inverted images shown in Fig. 2 has been performed and the resulting angular distributions have been fitted to Eq. (7), considering a one-photon dissociation process and a $(n+m)$ REMPI scheme[29–32]:

$$I(\theta) = \frac{\sigma}{4\pi} \sum_{i=0}^{2n+2} \beta_i P_i(\cos\theta)) \qquad (7)$$

where θ is the angle between the photofragment recoil velocity and the photolysis laser polarization direction, σ is the absorption cross section, β_i are anisotropy parameters which reflect the dissociation dynamics and the photofragment polarization, P_i are the Legendre polynomials of i-th order and n is the number of photons of the resonant step of the REMPI process. The $i=0$ term corresponds to the population of the studied species, and given that the experimental setup has not been calibrated for total intensities, the whole distribution is normalized to β_0, and the quotient is treated as a normalization fitting parameter. Up to three β_i anisotropy parameters would be expected to characterize the angular distributions in the present case. The index i takes only even values since we employ linearly polarized pump and probe

laser pulses. If no photofragment polarization is expected, Eq. (7) can however be truncated to $i=2$. Since H(^2S) atom fragments present a total angular momentum $J=1/2$, and the photolysis and probe lasers are linearly polarized, any alignment or orientation effects cannot be detected here and, therefore, a single β_2, henceforth β, is employed.

For all excitation wavelengths, the resulting β anisotropy parameter as a function of the H-atom speed is depicted in Figure 4. A similar behavior is observed at all excitation wavelengths: at low H-atom speeds, between ≈ 500 and ≈ 1250 m/s, the β parameter takes values around ≈ 0, consistent with an isotropic angular distribution. Such distribution is expected for slow dissociation processes, *i.e.* the reaction time is similar or larger than the rotational period of the molecule and, therefore, any angular information due to the initial transition is lost due to rotational motion of the molecule during dissociation. In contrast, at higher H-atom speeds, ≥ 1250 m/s, the β parameter shows negative values. Such anisotropic angular distributions reflect a second faster reaction pathway, characterized by an H-atom emission in a perpendicular direction with respect to the transition dipole moment which would depend on the symmetry of the excited state populated.x It is particularly interesting that this second mechanism, assigned to a prompt dissociation, seems to be observed in all the explored excitation region, even though different electronic excited states are initially populated. Direct excitation to $\widetilde{B}\,^2A_1$ from the ground electronic state is forbidden by symmetry while vibrational motion lead to allowed transitions by vibronic coupling. Vibronic bands of $\widetilde{B}\,^2A_1$ were indeed observed in the reported absorption spectra[15] and excitation at 243 nm directly populates the 11_0^1 band of $\widetilde{B}\,^2A_1$. The orientation of the transition dipole moment in that case would depend on the symmetry of the vibrational normal mode. In contrast, shorter wavelengths induce excitation to higher electronic states, in particular $\widetilde{C}\,^2B_2$ and $\widetilde{E}\,^2B_1$. The transition from the ground state to either of these two electronic states is characterized by a transition dipole moment perpendicular to the C-H bond located on the central C atom. The perpendicular angular distribution of the H-atom measured is in fact consistent with the population of these states if the major pathway (Eq.1) is considered. Based on a qualitative analysis of the β evolution in Fig. 4, the branching ratio for this pathway depends on the excitation wavelength and it appears to be particularly favorable at 243 nm. Taking this into account, this second mechanism could correspond to a prompt dissociation pathway involving in particular the $\widetilde{B}\,^2A_1$ excited state. At all other higher excitation energies, such prompt dissociation channel may then start by an efficient internal conversion from the higher excited states to the $\widetilde{B}\,^2A_1$ state. The three-state conical intersection between the $\widetilde{B}\,^2A_1$, $\widetilde{C}\,^2B_2$ and $\widetilde{D}\,^2A_1$ states reported by Yarkony and Matsika[23], and in particular the two-state linked conical intersection located close to the equilibrium geometry of the $\widetilde{B}$ state may play an important role in this mechanism. Further theoretical support would be particularly valuable in order to completely disentangle it. This second prompt pathway is, however, completely embedded in the main translational Boltzmann-type distribution and, thus, its branching ratio must be considerably small. The angular analysis permits nevertheless to unravel the presence of this
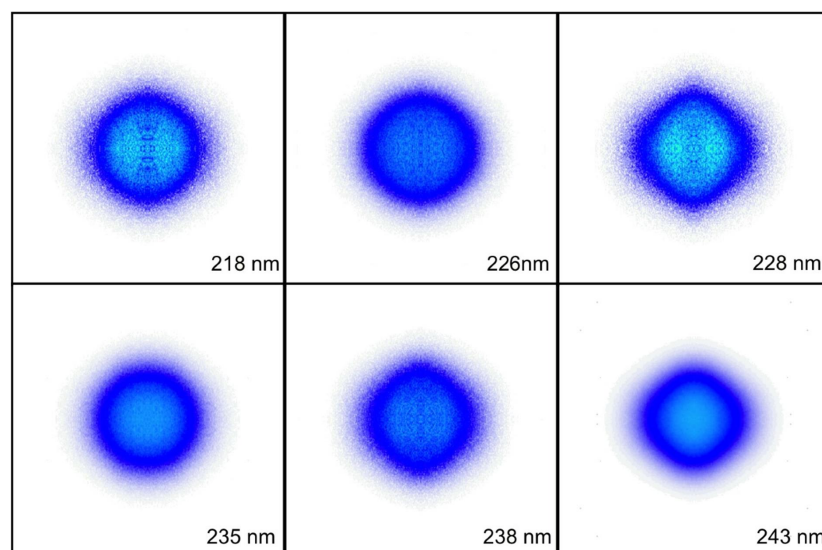
Fig. 2 Symmetrized VMI images of the H-atom fragment produced from the photodissociation of the allyl radical at selected excitation wavelengths between 218 and 243 nm employing a (2+1) REMPI scheme at 243.12 nm for detection. The probe contribution and pyrolytic background have been subtracted.

prompt dissociation highlighting the power of the angular analysis to assign different dissociation mechanisms. Such power to disentangle different reaction pathways has been demonstrated in the past, for instance in the nitromethane photodissociation.[33]

3.2 The CH$_3$ elimination channels

A series of raw VMI images of CH$_3$(v=0) fragments from the photodissociation of the allyl radical at different photolysis wavelengths, ranging between 216 and 240 nm and detected via (2+1) REMPI are displayed in Figure. 5. The contribution of the probe pulse, the pump pulse and the background signal associated to the pyrolytic source have been carefully subtracted from the images. The pump-probe signal represents around 1.5 times the probe contribution, while the background signal is lower and the pump one is non-negligible but minimal. For $\lambda \leqslant 230$ nm, images have been recorded in different days and carefully added to increase the statistics. The raw images prior subtraction at 216 nm are shown as an example in the ESI. A set of ZZ images were similarly recorded and employed to rule out any significant inhomogeneity in the detector. In general terms, the signal is very low at practically all the excitation wavelengths, which reflects that the CH$_3$ elimination channels are really minor in comparison with the H-atom elimination channels in the photodissociation of the allyl radical.

Two different trends are clearly observed in the images as excitation energy decreases. At shorter excitation wavelengths, a broad isotropic ring is observed, which gets significantly broader as excitation wavelength increases from 216 nm up to 230 nm. In contrast, a small isotropic blot is recovered at longer wavelengths – 238 and 240 nm – *i.e.* at the lowest excitation energies. We remark as commented on above that the signal is particularly low, which indicates a small formation of the methyl fragment in its vibrational ground state from allyl photodissociation in the explored excitation energy region. Besides, increasing the excitation energy entails a surprising remarkable decrease of the recorded signal intensity, although the general low signal-to-noise ratio at all excitation wavelengths studied make difficult to quantify it. Since only measuring CH$_3$(v=0) fragments may give an incomplete perspective on the dissociation pathways, experiments were performed at the excitation wavelength λ_{exc}=230 nm, detecting CH$_3$(v_1=1) and CH$_3$(v_2=1) employing (2+1) REMPI schemes at 333.9 nm and 329.5 nm, respectively. A rather significantly weaker signal compared to the CH$_3$($v = 0$) fragment signal was obtained for these vibrationally excited species. The images apparently show a component in the low energy region (not shown here) even though the signal-to-noise ratios in those cases were remarkably low.

The translational energy distributions obtained from the angular integration of the VMI images are depicted in Figure 6. We note that these TEDs are rather noisy due again to the low signal-to-noise ratio of the measured images, *i.e.* a particularly low amount of CH$_3$(v=0) is produced in the photodissociation of
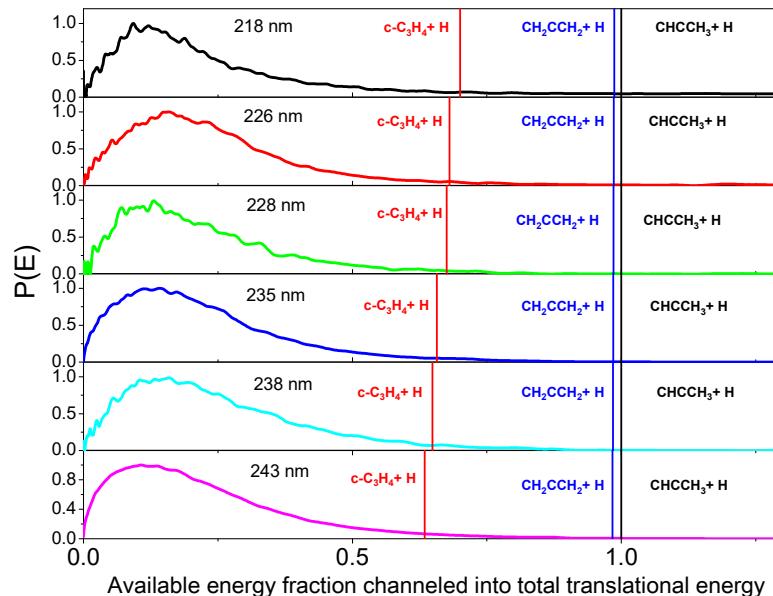
Fig. 3 Translational energy distributions of the H-atom fragment represented as a function of the available energy fraction appearing as total translational energy at different excitation wavelengths in the range 218-243 nm obtained by angular integration of the corresponding Abel-inverted images shown in Fig. 2. The X-axis has been normalized to the available energy of the CH_3CCH + H channel. The vertical bars represent the corresponding available energy E_{av} for the three opened dissociation channels c-C_3H_4 + H, CH_2CCH_2 + H and CH_3CCH + H as indicated.

the allyl radical. As in the case of the H-atom elimination channels, the energy axis has been normalized, in this case, to the available energy of the HCCH + CH_3 dissociation limit with D_0 = 2.00 eV.[19] In agreement with the images, at shorter excitation wavelengths, a broad contribution at higher translational energies is observed, becoming broader with increasing wavelength. In addition, the maximum, located between $E_T \approx 1.75$ and ≈ 2.25 eV is shifted towards lower translational energies as the excitation wavelength increases. In contrast, at 238 nm and 240 nm, a narrow distribution at threshold translational energies is recovered. The images and the corresponding TEDs clearly reflect two different dissociation pathways, depending on the excitation energy, leading to the formation of $CH_3(v=0)$.

The analysis of the anisotropy has been similarly carried out through a pixel-to-pixel integration of the $CH_3(v = 0)$ images. The corresponding angular distributions have been analyzed using Eq. (7). Since the methyl radical might show rotational angular momentum alignment, the three β_2, β_4 and β_6 parameters have been employed in the fit. In all cases, β_4 and β_6 present however nearly zero values taking into account the experimental error. This would indicate that the methyl fragment is not affected by strong polarization effects although the low signal-to-noise ratio precludes a definitive conclusion. The evolution of β_2 as a function of the $CH_3(v=0)$ speed is depicted in Figure 7. The low $CH_3(v=0)$ signal makes particularly difficult to reliably measure the anisotropy of the angular distributions. An approximate average value and a qualitative tendency may be extracted, however. All distributions mainly show values of $\beta_2 \approx 0$, which reflects

that the formation of $CH_3(v=0)$ in the whole explored range of excitation energies is governed by statistical processes.

In order to unravel the different reaction pathways, the translational energy distributions obtained in this work for the CH_3 fragment have been compared with the results of quasi-classical trajectory calculations carried out by Stranges and co-workers performed at 248 nm.[20,21] This comparison is depicted in Figure 8, where in the top panel the present results at 216 and 230 nm, reflecting a broad contribution in the TEDs, are compared to three selected theoretical distributions from Ref.[20] corresponding to trajectories: (*i*) from the global minimum (GM) into the CH_3 + HCCH fragments, *via* Eq. (4) (*i.e.* a single 1,3-hydrogen shift), (*ii*) from LM2 (*i.e.* paths (4) and (5)), and (*iii*) from LM1 but subtracting the vinylidene channel *via* Eq. (6) (*i.e.* pathway (5)).

In contrast, the results recorded at 238 and 240 nm, characterized by a threshold-energy peak in the TEDs, are displayed in the bottom panel of Fig. 8 along with two theoretical distributions for the trajectories: (*i*) from the GM into the CH_3 + HCCH fragments, *via* Eq. (5) (*i.e.* two 1,2-hydrogen shifts), and (*ii*) from LM1 including the vinylidene channel (pathway (6)).

The experimental results are in considerably good agreement with the theoretical distributions and, thus, the two different pathways assigned in the two excitation regions can be unraveled. Firstly, at shorter wavelengths, between 216 and 230 nm, the TEDs are consistent with pathway (4) (top panel, solid blue line) with some contribution from pathway (5). The comparison between trajectories from LM2 into both pathways (4) and (5) and from LM1 into pathway (5) highlights a TED distribution located
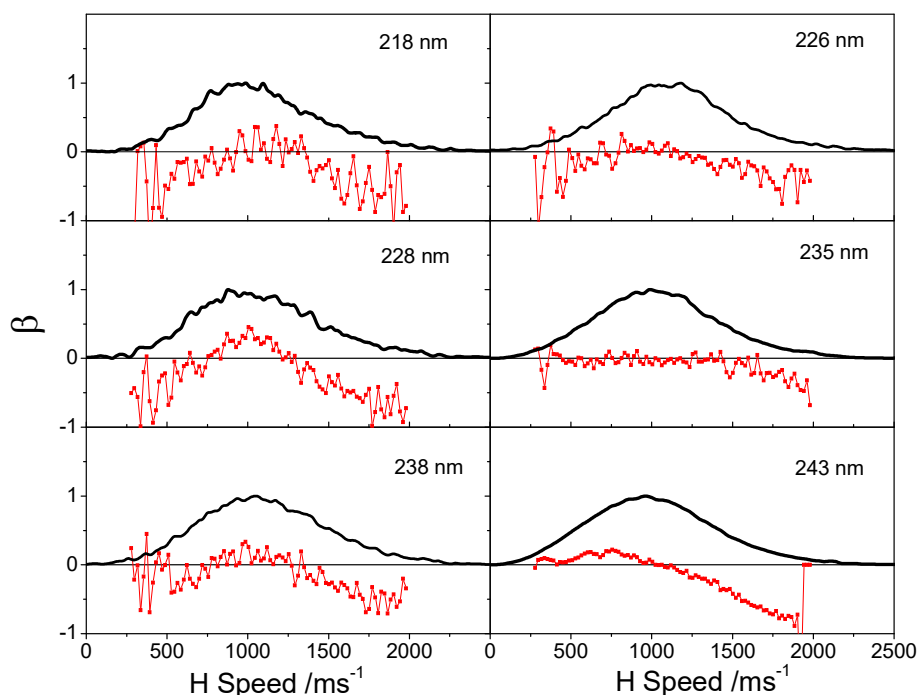
Fig. 4 Anisotropy parameter β as a function of the H-atom fragment speed (red squares and traces) for the different excitation wavelengths studied. The corresponding speed distribution of the H-atom is shown as a visual guide (black curves).

at slightly higher energies for pathway (5). The relative contribution of both pathways (4) and (5) might then contribute to the evolution of the experimental TEDs in this excitation energy region. At higher excitation energies (216 and 218 nm), pathway (5) would be more favorable, in agreement with the sharper ring observed at higher radius in the images (see Fig. 5), while at lower excitation energies (220 and 230 nm), the branching ratio for pathway (4) increases leading to the broader experimental TED.

In the second excitation energy region, at longer wavelengths (Fig. 8, bottom) (238-240 nm), qualitative agreement is obtained between the experiment and the trajectory calculations, including pathways (5) and (6). In contrast to the trajectories from LM1 in the top panel, the ones shown here include the two pathways: *via* two 1,2-hydrogen shifts (pathway (5)) and *via* the vinylidene (pathway (6)). Taking into account that the distribution from LM1 through Eq. (5) is consistent with a broader energy distribution (see top panel), the experimental distribution at threshold energies seems to be consistent with a major dissociation *via* the vinylidene channel (pathway (6)) and a small contribution from pathway (5).

The results at 240 and 238 nm are in excellent agreement with the previous experimental results following excitation at 248 nm by the Stranges group.[19] The branching ratio for the vinylidene channel seems, however, to remarkably increase at the present wavelengths, 240 and 238 nm, based on a qualitative comparison. In the present work, the TEDs show a sharper contribu-

tion at threshold energies, while at 248 nm the TED is slightly shifted to larger energies. The threshold energy distribution was indeed rationalized as the result of the formation of vinylidene with a large degree of vibrational energy, leaving a small amount of energy available. Such internal energy would permit further isomerization of vinylidene into HCCH (see Fig. 1).

The major role of the vinylidene channel, located at 1.16 eV above the TS4 transition state, indicates a strong coupling between the potential energy surface of the electronic state initially populated and the ground state in the vicinity of the TS5 leading to the CCH$_2$ formation. Such coupling may be stronger between the $\widetilde{C}\,^2A_2$ state initially populated at 240 and 238 nm than with the $\widetilde{B}\,^2A_1$ state excited at 248 nm. TS5 was already considered a very *loose* transition state, over the relatively *tight* transition state TS4, explaining the relevant role of the vinylidene channel despite its higher energy transition state[20]. In addition, the branching ratio for this channel (Eq. (6)) was predicted to increase with excitation energy.

It is noteworthy to point out, however, the existing discrepancy with regard to the time scales published in the literature. The trajectory calculations referred to here provide a dissociation time of $\approx$16 ps and a dissociation rate of 6.3×10^{10} s^{-1}, while the dissociation rate of the allyl radical measured by Deyerl and co-workers[16,18] using time- and frequency-resolved photoionization of hydrogen atoms with α-Lyman radiation, are two orders of magnitude smaller (4.8×10^8 s^{-1}), *i.e.* reflecting a longer dissociation time. Besides, Deyerl and co-workers reported variations

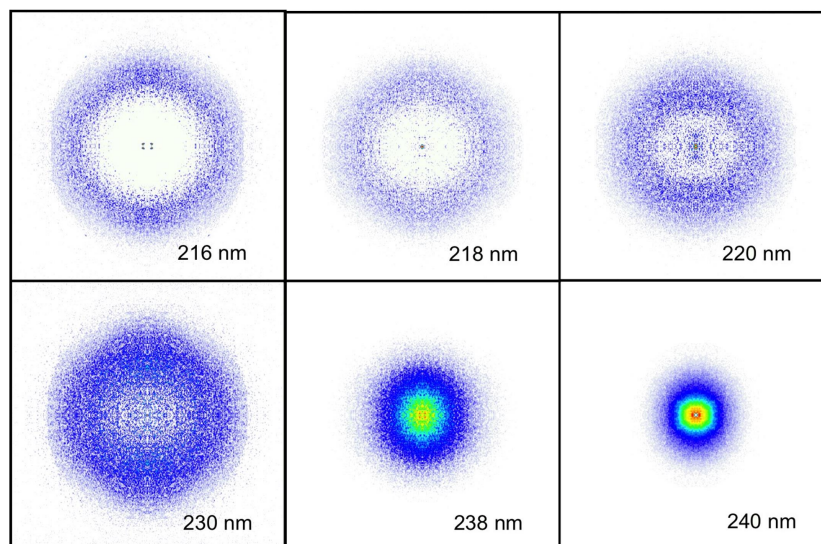**Fig. 5** Symmetrized VMI images of the $CH_3(v=0)$ fragment from the allyl radical photodissociation at selected excitation wavelengths between 216 and 240 nm employing a (2+1) REMPI scheme at 333.45 nm (see text for more details). The probe contribution, pump contribution and pyrolytic background signal have been carefully subtracted.

in the H/D ratio of the 2-deuteroallyl species of up to 100 ns. As pointed out by the authors, the source of the discrepancy could be related to the fact that although at 248 nm the radical is excited into the $\widetilde{B}$ state, the trajectory calculations of Stranges and co-workers start in the ground potential energy surface. Such approach might be inappropriate due to the complex interactions of the different states involved in the process. The interpretation made here based on the comparison of our experimental results with these trajectory calculations is, therefore, somewhat limited.

Taking into account the theoretical results from Ref.[20,21], it is nevertheless surprising the change of mechanism observed at higher excitation energies (shorter wavelengths λ_{exc}). For wavelengths shorter than 230 nm, the vinylidene channel does not seem to play a significant role anymore, while methyl formation arises mainly from a single 1,3-hydrogen shift or a double 1,2 shift, pathways (4) and (5), respectively.

This is in striking contradiction with one of the main conclusions of Stranges and co-workers, who predicted an increasing contribution from pathway (6) at higher excitation energies. Two main reasons can explained this contradiction. At $\lambda_{exc} \leq 230$ nm, the initial excitation leads to the population on the $\widetilde{E}\ ^2B_1$. This state could either be efficiently coupled to the ground state in the region of the TS1, TS2 or even TS4 transition states, but not around TS5, or not be coupled to the ground state in any transition state region. In the latter case, the excited allyl radical would probably end up by decaying into LM1 and further dissociating through pathways (4) or (5). In the first case, the change of mechanism should go along with a strong increase of the signal with decreasing λ_{exc}, while in the second case, since the decay to

the ground state would be produced statistically, a decrease of the signal would be expected. The present results and, in particular, the signal-to-noise ratio in the methyl images depicted in Fig. 5, point towards the second possibility: the $\widetilde{E}$ state is not coupled to the ground state for geometries close to any transition state and a rather slow decay into LM1 leads to dissociation. In this context, the dynamics on this higher excited state seems to be quite different from the dynamics at the lower electronic states, which are presumed to undergo rather efficient internal conversion to the ground state prior slow dissociation.

For $\lambda_{exc} \leq 230$ nm, the vinylidene channel could be nevertheless produced in coincidence with vibrationally excited methyl fragments, and therefore, not being observed in the present experiments. Although our measurements do not indicate a remarkable formation of $CH_3(v_1=1)$ or $CH_3(v_2=1)$ and, thus, a strong inversion of population is rather unlikely, further measurements detecting the whole vibrational distribution of methyl fragments would be necessary.

4 Conclusions

The photodissociation of the allyl radical following excitation between 216 and 243 nm has been investigated employing velocity map imaging in combination with resonant enhanced multiphoton ionization to detect the hydrogen atoms and $CH_3(v=0)$ fragments produced. The translational energy distributions for the two fragments are reported and analyzed along with the corresponding angular distributions. The results are discussed in terms of the different reaction pathways characterizing the hydrogen-atom elimination and the minor methyl formation.
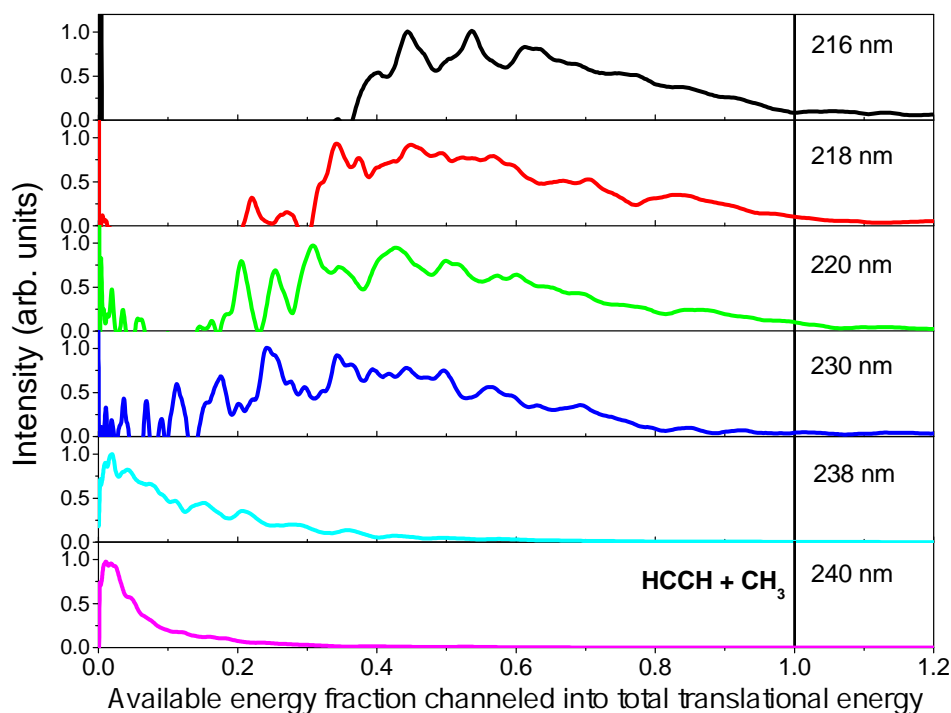
Fig. 6 Translational energy distributions of the $CH_3(\nu=0)$ fragment represented as a function of the available energy fraction appearing as total translational energy at different excitation wavelengths in the range 216-240 nm obtained by angular integration of the corresponding Abel-inverted images shown in Fig. 5. The X-axis has been normalized to the available energy of the $HCCH + CH_3$ channel.

The translational energy distributions measured for the hydrogen atoms are consistent with the main formation of CH_2CCH_2 + H and $CHCCH_3$ + H, and a minor contribution of the c-C_3H_4 + H channel, which increases with the excitation energy, in agreement with previous results. The evolution of the anisotropy parameter as a function of the H-atom speed provides, however, evidence of an additional mechanism, not reported before, leading to prompt dissociation and fast hydrogen atoms.

The methyl elimination channel has been characterized as a function of the excitation energy and the contribution of three reaction pathways, through one single 1,3-hydrogen shift, through a double 1,2-hydrogen shift or through the formation of vinylidene has been discussed. Contrary to previous predictions, the vinylidene channel, which plays a significant role at lower energies seems to vanish following excitation to the $\widetilde{E}\ ^2B_1(3p_x)$ excited state at $\lambda_{exc} \leq 230$ nm.

Conflicts of interest

There are no conflicts to declare.

Acknowledgements

Notes and references

1 X. B. G, Y. Guo, F. T. Zhang, A. M. Mebel and R. I. Kaiser, *Faraday Discussions*, 2006, **133**, 245.

2 T. Owen, *Nature*, 2005, **438**, 756.

3 P. R. Mahaffty, *Science*, 2005, **308**, 969.

4 K. M. Leung and R. P. Lindstedt, *Combust. Flame*, 1995, **102**, 129.

5 J. A. Miller, R. J. Kee and C. K. Westbrook, *Annu. Rev. Phys. Chem.*, 1990, **41**, 345.

6 N. M. Marinov, M. J. Castaldi, C. F. Melius and W. Tsang, *Combust. Sci. Technol.*, 1997, **128**, 295.

7 J.P.Senosiain, C. J.H.Han and D.M.Golden, *FaradayDiscuss.*, 2001, **119**, 173.

8 N. Hansen, W. Li, M. E. Law, T. Kasper, P. R. Westmoreland, B. Yang, T. A. Cool and A. Lucassen, *Physical Chemistry Chemical Physics*, 2010, **12**, 12112–12122.

9 J. A. Miller, S. J. Klippenstein, Y. Georgievskii, L. B. Harding, W. D. Allen and A. C. Simmonett, *The Journal of Physical Chemistry A*, 2010, **114**, 4881–4890.

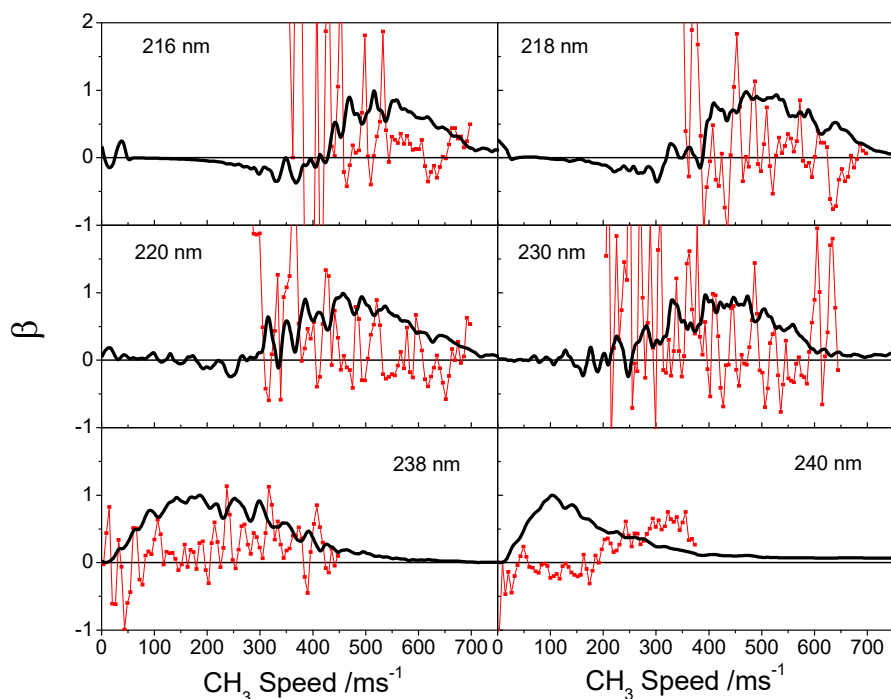10 C. Currie and D. Ramsay, *The Journal of Chemical Physics*,

Fig. 7 Anisotropy parameter β as a function of the CH_3 fragment speed (red squares and traces) for the different excitation wavelengths. The corresponding speed distributions of CH_3 are shown as a visual guide (black curves).
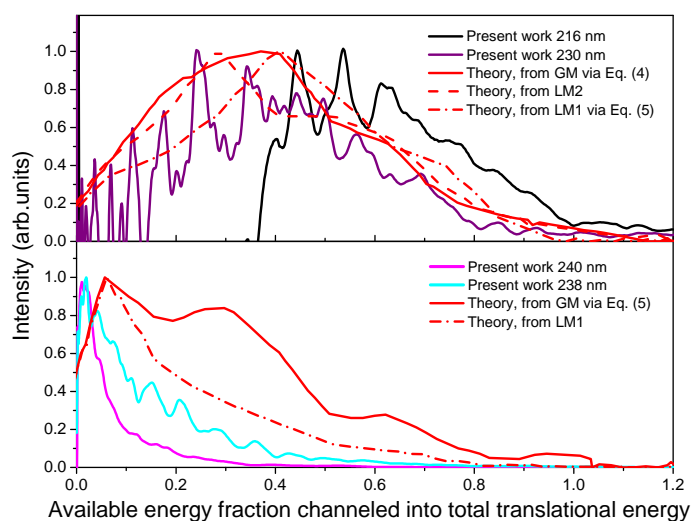

Fig. 8 Comparison between the CH_3 fragment translational energy distributions obtained in the present work and those obtained from quasiclassical trajectory calculations by Stranges and co-workers at 248 nm [20]. The abscissa axis has been normalized to the available energy for the CH_3 + HCCH dissociation channel. Top: Experimental distributions obtained at 216 and 230 nm; trajectories from the GM through Eq. (4) (solid red line), from LM2 *via* pathways (4) and (5) (dashed red line), and from LM1 through Eq. (5) (dashed-dot red line). Bottom: Experimental distributions obtained at 238 and 240 nm; trajectories from the GM *via* Eq. (5) and from LM1.

1966, **45**, 488–491.

11 J. W. Hudgens and C. Dulcey, *The Journal of Physical Chemistry*, 1985, **89**, 1505–1509.

12 A. Callear and H. Lee, *Transactions of the Faraday Society*, 1968, **64**, 308–316.

13 D. W. Minsek, J. A. Blush and P. Chen, *The Journal of Physical Chemistry*, 1992, **96**, 2025–2027.

14 M. Gasser, A. M. Schulenburg, P. M. Dietiker, A. Bach, F. Merkt and P. Chen, *The Journal of chemical physics*, 2009, **131**, 014304.

15 M. Gasser, J. A. Frey, J. M. Hostettler, A. Bach and P. Chen, *The Journal of Physical Chemistry A*, 2010, **114**, 4704–4711.

16 H. J. Deyerl, T. Gilbert, I. Fischer and P. Chen, *Journal of Chemical Physics*, 1997, **107**, 3329.

17 D. Stranges, M. Stemmler, X. Yang, J. D. Chesko, A. G. Suits and Y. T. Lee, *J. Chem. Phys.*, 1998, **109**, 5372.

18 H. J. Deyerl, I. Fischer and P. Chen, *Journal of Chemical Physics*, 1999, **110**, 1450.

19 D. Stranges, P. O'Keeffe, G. Scotti, R. Di Santo and P. L. Houston, *The Journal of Chemical Physics*, 2008, **128**, 151101.

20 C. Chen, B. Braams, D. Y. Lee, J. M. Bowman, P. L. Houston and D. Stranges, *The Journal of Physical Chemistry Letters*, 2010, **1**, 1875–1880.

21 C. Chen, B. Braams, D. Y. Lee, J. M. Bowman, P. L. Houston and D. Stranges, *J. Phys. Chem. A*, 2011, **115**, 6797.

22 Y. Song, M. Lucas, M. Alcaraz and J. Zhang, *J.Phys.Chem.A*, 2015, **119**, 12318.

23 S. Matsika and D. R. Yarkony, *Journal of the American Chemical Society*, 2003, **125**, 10672–10676.

24 L. Rubio-Lago, A. García-Vela, A. Arregui, G. A. Amaral and L. Bañares, *J. Chem. Phys.*, 2009, **131**, 174309.

25 S. M. Poullain, D. V. Chicharro, A. Zanchet, M. G. González, L. Rubio-Lago, M. L. Senent, A. García-Vela and L. Bañares, *Physical Chemistry Chemical Physics*, 2016, **18**, 17054–17061.

26 D. W. Kohn, H. Clauberg and P. Chen, *J. Chem. Phys.*, 1992, **63**, 4003.

27 L. Castiglioni, *PhD thesis*, Swiss Federal Institute of Technology ETH Zürich, 2007.

28 V. Papadakis and T. N. Kitsopoulos, *Rev. Sci. Instrum.*, 2006, **77**, 083101.

29 R. N. Dixon, *J. Chem. Phys.*, 1986, **85**, 1866.

30 T. P. Rakitzis, *Chem. Phys. Lett.*, 2001, **342**, 121.

31 T. P. Rakitzis and R. N. Zare, *J. Chem. Phys.*, 1999, **110**, 3341.

32 R. N. Zare, *R. N. Zare*, 1998, vol. Angular Momentum: Understanding Spatial Aspects in Chemistry and Physics.

33 J. Rodríguez, M. González, L. Rubio-Lago, L. Bañares, P. Samartzis and T. Kitsopoulos, *The Journal of Physical Chemistry A*, 2013, **117**, 8175–8183.